JGR Oceans

RESEARCH ARTICLE
10.1029/2019JC015526

# Observations of Turbulence at a Near-Surface Temperature Front in the Arctic Ocean

**Zoé Koenig[1,2], Ilker Fer[1], Eivind Kolås[1], Trygve O. Fossum[3], Petter Norgren[3], and Martin Ludvigsen[3]**

[1]Geophysical Institute and Bjerknes Center for Climate Research, University of Bergen, Bergen, Norway, [2]Norwegian Polar Institute, Tromsø, Norway, [3]Department of Marine Technology, Norwegian University of Science and Technology, Trondheim, Norway

**Key Points:**
- Strong lateral and vertical variability was observed at an ocean front close to the sea ice edge in the Nansen Basin
- Surface buoyancy fluxes and wind stress were the main sources of turbulence in the mixed layer
- Conditions were favorable for forced symmetric instability, which could contribute to increase turbulence below the mixed layer

**Correspondence to:**
Z. Koenig,
zoe.koenig@uib.no

**Citation:**
Koenig, Z., Fer, I., Kolås, E., Fossum, T. O., Norgren, P., & Ludvigsen, M. (2020). Observations of turbulence at a near-surface temperature front in the Arctic Ocean. *Journal of Geophysical Research: Oceans*, *125*, e2019JC015526. https://doi.org/10.1029/2019JC015526

Received 26 JUL 2019
Accepted 2 MAR 2020
Accepted article online 10 MAR 2020



**Abstract** High-resolution ocean temperature, salinity, current, and turbulence data were collected at an Arctic thermohaline front in the Nansen Basin. The front was close to the sea ice edge and separated the cold and fresh surface melt water from the warm and saline mixed layer. Measurements were made on 18 September 2018, in the upper 100 m, from a research vessel and an autonomous underwater vehicle. Destabilizing surface buoyancy fluxes from a combination of heat loss to the atmosphere and cross-front Ekman transport by down-front winds reduced the potential vorticity in the upper ocean. Turbulence structure in the mixed layer was generally consistent with turbulence production through convection by heat loss to atmosphere and mechanical forcing by moderate winds. Conditions at the front were favorable for forced symmetric instability, a mechanism drawing energy from the frontal geostrophic current. A clear signature of increased dissipation from symmetric instability could not be identified; however, this instability could potentially account for the increased dissipation rates at the front location down to 40 m depth that could not be explained by the atmospheric forcing. This turbulence was associated with turbulent heat fluxes of up to 10 W $m^{-2}$, eroding the warm and cold intrusions observed between 30 and 60 m depth. A Seaglider sampled across a similar frontal structure in the same region 10 days after our survey. The submesoscale-to-turbulence-scale transitions and resulting mixing can be widespread and important in the Atlantic sector of the Arctic Ocean.

**Plain Language Summary** On 18 September 2018, high-resolution temperature, salinity, current, and turbulence data were collected near a surface temperature and salinity front in the Nansen Basin north of Svalbard, within the framework of the Nansen Legacy Project. Measurements were performed from the research icebreaker Kronprins Haakon and using an autonomous underwater vehicle. The front separates warm and salty Atlantic-origin waters from cold and fresh Arctic-origin waters. Energetic turbulence in the upper 30 m was consistent with convection by heat loss to the atmosphere and mechanical forcing by moderate winds at the surface of the ocean. At the front, the conditions were favorable for forced symmetric instability, a mechanism drawing energy from the large-scale current. The contribution to turbulence from this instability could not be clearly identified but can be potentially important. Such observations linking 1–3 km scales to turbulence in the Arctic Ocean are rare. Turbulence at a front in the Arctic has consequences on the heat and nutrient transport from the slope to the deep Arctic Basin. A Seaglider sampled across a similar frontal structure in the same region end of September 2018. Observed frontal structure and mixing processes can be common in the Atlantic sector of the Arctic Ocean.

## 1. Introduction

Warm Atlantic Water is the main source of oceanic heat to the Arctic Ocean (Carmack et al., 2015; Rudels et al., 2015). Among the two main Atlantic Water pathways into the Arctic through Fram Strait and the Barents Sea, the Fram Strait inflow mainly remains in the Nansen Basin while the Barents Sea inflow continues along the continental slope, enters the Amundsen Basin, and provides most of the Atlantic Water in the Makarov and Canada basins (Aagaard, 1989). As the Atlantic Water boundary current flows cyclonically along the upper continental slope, it mixes vertically and laterally, spreading its heat to the interior Arctic basins; the processes of vertical and lateral mixing, however, are not well understood (Carmack et al., 2015).

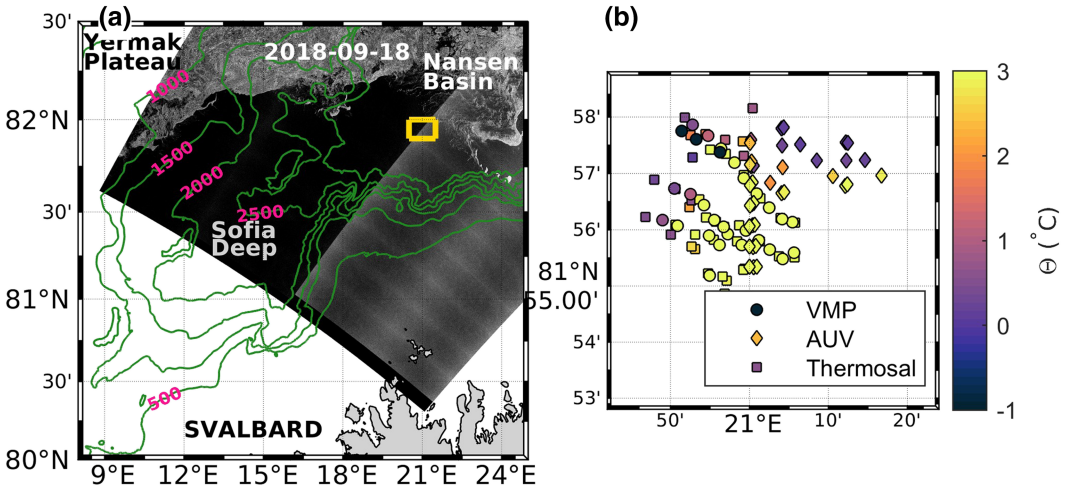


**Figure 1.** (a) Sentinel 1 image taken on 18 September 2018, north of Svalbard. The lighter regions are covered with sea ice while the dark colors correspond to open ocean. Bathymetry contours from the International Bathymetric Chart of the Arctic Ocean, IBCAO-v3 (Jakobsson et al., 2012) are shown at 500-m intervals (green). The yellow rectangle is the location of the front study expanded in (b). (b) Station map for the front study showing the location of microstructure (VMP, circles), AUV (diamonds), and thermosalinograph (30 min averaged, squares) data, all color-coded for near-surface temperature.

In the Arctic Ocean, vertical mixing is typically dominated by turbulence generated by processes over topography and along margins, mainly forced by tides (Fer et al., 2015; Lenn et al., 2011; Padman & Dillon, 1991; Rippeth et al., 2015). In the central Arctic, sea ice limits the energy input from wind, and the vertical mixing is weak (Fer, 2009; Rainville & Winsor, 2008). Vertical stratification is favorable for double diffusive processes driven by the differing molecular diffusivities of heat and salt, and thermohaline staircases are widespread (Padman & Dillon, 1987; Shibley et al., 2017). Double diffusive heat fluxes are, however, weak about 0.1 to 1 W $m^{-2}$ in the central Arctic (Guthrie et al., 2013; Sirevaag & Fer, 2012) and 1 to 10 W $m^{-2}$ in the eastern Arctic Ocean (Polyakov et al., 2019). Episodic energetic vertical mixing in the interior ocean has been observed in response to strong winds and ice divergence. Upwelling of warm Atlantic waters in the central Arctic led to vertical fluxes of 100 W $m^{-2}$ (McPhee, 1992). Near 89°N, increased dissipation rates have been recorded in the pycnocline following strong winds, coherent with energized near-inertial internal waves (Fer, 2014). North of Svalbard, winter storms increased the pycnocline fluxes by a factor of 2 (Meyer, Fer, et al., 2017) and the ocean-to-ice fluxes by a factor of 3 (Graham et al., 2019).

Lateral mixing and spreading of Atlantic Water have been associated with thermohaline intrusions (Rudels et al., 2000) and stirring and mixing by mesoscale eddies (Crews et al., 2018; D'Asaro, 1988; Dosser & Timmermans, 2018; Manley & Hunkins, 1985; Padman et al., 1990). Analyzing Arctic-wide temperature and salinity profiles collected over the past decade, Zhao et al. (2014) described a prevalent Arctic eddy field, typically generated by instability of surface fronts (in the eastern Canada basin) or instability of boundary currents (in the southwestern Canada Basin or in the vicinity of ridges and the Eurasian Basin shelves). Using an inverse method and repeat hydrographic measurements between 2003 and 2015, Dosser and Timmermans (2018) estimated along-isopycnal diffusivity in the Canada Basin to be 300–600 $m^2$ $s^{-1}$. Using high-resolution measurements from an intrahalocline eddy on the Chukchi slope, Fine et al. (2018) quantified contribution of different processes to the heat loss of the eddy. At the top edge of the eddy, double diffusion led to an upward heat flux of 5 W $m^{-2}$, at the bottom edge shear-driven mixing generated a downward heat flux of 0.5 W $m^{-2}$, and along the sides density-compensated thermohaline intrusions transported 2,000 W $m^{-2}$ laterally out of the eddy.

Temperature and salinity fronts in the upper Arctic Ocean are common, associated with, for example, currents separating different water masses, melt, and growth cycle of sea ice, advection of sea ice, surface warming across variable sea ice cover, and so forth. Because of strong lateral gradients, such frontal systems host complex dynamical processes that affect the evolution and stratification of the mixed layer. Turbulence observations in Arctic fronts, however, are rare. Fer and Drinkwater (2014) studied the Barents Sea polar front where the front was quiescent beneath a turbulent surface layer. Biological activity was elevated

between the polar front and a tidally generated front over shallows where tidal mixing effectively mixed the nutrient rich deep water upward, sustaining the phytoplankton bloom. At midlatitudes, in a coastal upwelling front in the California Current, Johnston et al. (2011) observed elevated subsurface mixing and a deep chlorophyll and biomass maximum on the dense side of the front, likely related to energy cascade from mesoscale to microscale.

At a front, submesoscale processes allow efficient downscale energy cascade from balanced flows to turbulence through various instabilities depending on the vorticity, stratification, or baroclinicity of fluid (D'Asaro et al., 2011; Thomas et al., 2013). While these processes are well described at midlatitudes and energetic frontal systems such as the Gulf Stream (Thomas et al., 2013), observations in the Arctic Ocean are rare despite the common presence of frontal regions.

In this study we present detailed observations characterizing the structure of hydrography, currents, and turbulence at a near-surface front in the Arctic Ocean in the Nansen Basin away from topography, 4–5 km away from the sea ice edge (Figure 1a).

## 2. Data

Data were collected during a cruise onboard the Norwegian icebreaker *R/V Kronprins Haakon* (12–24 September 2018) within the framework of the Nansen Legacy (Fer et al., 2019). Extensive measurements were made on 18 September 2018 for a duration of 24 hr at a front in the Nansen Basin, in the Sofia Deep north of Svalbard (81.9°N, 21°E), 4–5 km south of the sea ice edge (Figure 1a). From the ship, data were collected using a thermosalinograph, a vertical microstructure profiler (VMP) and a ship-mounted acoustic Doppler current profiler (SADCP) for horizontal currents. A second set of data was collected independently from the ship using an AUV (autonomous underwater vehicle) equipped with conductivity, temperature, depth (CTD), dissolved oxygen, and fluorescence sensors. The ship and the AUV were not colocated (Figure 1b) to avoid any risk of collision. To collect shipboard microstructure measurements across the front, the front was first detected from a thermosalinograph transect. Then, the ship was positioned on the upwind side of the front, and the VMP profiles were collected as the ship drifted across the front. After two to three stations on the downwind side of the front, the ship was relocated upwind to start a new drift. The cross-front extent of the survey (about 5 km, Figure 1b) was limited by the operational constraints of the AUV. We describe the data from each instrument in the following subsections. We use the International Thermodynamic Equations of Seawater (TEOS-10), (McDougall & Barker, 2011) with conservative temperature ($\Theta$) and absolute salinity ($S_A$).

### 2.1. Microstructure Measurements

A 2,000 m-rated VMP manufactured by Rockland Scientific, Canada (RSI), was used. The VMP is a loosely tethered profiler with a nominal fall speed of 0.6 m $s^{-1}$ . The profiler was equipped with pumped Sea-Bird Scientific (SBE) CT sensors, a pressure sensor, airfoil velocity shear probes, one high-resolution temperature sensor, one high-resolution microconductivity sensor, and three orthogonal accelerometers. The microstructure data were processed using the routines provided by RSI (ODAS v4.01). Assuming isotropic turbulence, the dissipation rate of turbulent kinetic energy per unit mass, $\epsilon$, can be expressed as

$$\epsilon = 7.5\nu\overline{\left(\frac{\partial u}{\partial z}\right)^2}, \tag{1}$$

where $\nu$ is the kinematic viscosity, overbar denotes averaging in time, and $\partial u/\partial z$ is the small-scale shear of one horizontal velocity component $u$. Dissipation rates were calculated from the shear variance obtained by integrating the shear vertical wave number spectra in a wave number range that is relatively unaffected by noise and corrected for the variance in the unresolved portions of the spectrum using an empirical model (Nasmyth, 1970). The shear spectra were computed using 1 s Fourier transform length and half-overlapping 4 s segments.

Resulting values were quality screened by inspecting the instrument accelerometer records, individual spectra, and individual dissipation rate profiles from the two shear probes. Estimates from both probes were averaged, except when their ratio exceeded 10; for example, as a result of plankton hitting a sensor, the lowest estimate was chosen. Noise level of the dissipation rate measured by the VMP2000 is about $2-3\times10^{-10}$ W $kg^{-1}$. The temperature and salinity data from the VMP were compared against the ship's SBE

CTD profiles. A small offset of 0.002 g $kg^{-1}$ was applied to the salinity of the VMP. In total, 31 profiles were collected. Dissipation measurements from the upper 15 m were excluded because of the disturbance from the ship's keel, and the profiler's adjustment to free fall.

The turbulent heat flux $F_H$ was calculated as

$$F_H = -\rho_0 C_p K_\rho \frac{\partial \Theta}{\partial z}, \tag{2}$$

where $\rho_0 = 1{,}027$ kg $m^{-3}$ is the seawater density, $C_p = 3{,}991.9$ J·$kg^{-1}$·$K^{-1}$ is the specific heat of seawater, $\Theta$ is the background temperature, and $K_\rho$ is the diapycnal eddy diffusivity. We thus assume that turbulence diffuses the finescale temperature gradient at the same rate as the density gradient. The sign convention is that positive heat fluxes correspond to upward heat fluxes in the water column. An upper bound for diapycnal diffusivity was obtained using the Osborn (1980) relation:

$$K_\rho = \Gamma \frac{\epsilon}{N^2}, \tag{3}$$

with the mixing coefficient set to $\Gamma = 0.2$, the recommended value for the oceanic applications (Gregg et al., 2018). The buoyancy frequency or Brunt-Väisälä frequency, $N$, was calculated using $N^2 = -\frac{g}{\rho_0}\frac{\partial \sigma_\Theta}{\partial z}$, where $g$ is the gravitational acceleration and $\sigma_\Theta$ is the potential density anomaly. Background vertical gradients (for temperature and density) were taken over a 10 m-length scale. As $N$ approaches neutral stratification $K_\rho$ attains very large values. The estimates of $K_\rho$ in segments with buoyancy frequency below a noise level of $N^2 = 10^{-7}$ $s^{-2}$ were excluded.

### 2.2. Autonomous Underwater Vehicle

The AUV was deployed to autonomously collect high-resolution data across the front using adaptive sampling; see, for example, Fossum et al. (2018). Both front detection and sampling location were decided by a state-based autonomous agent running onboard the AUV, optimizing data collection across and along the front. The sampling platform was a light AUV (Sousa et al., 2012) equipped with an active pumping 16 Hz SBE 49 FastCAT CTD, an Anderaa Optode 4831 sensor (measuring the dissolved oxygen), and a WetLabs Triple-Measurement Meter EcoPuck (measuring color dissolved organic matter at 370/460 nm, chlorophyll *a* fluorescence at 470/695 nm, and optical backscatter). The accuracy of the CTD instrument is $\pm 3 \times 10^{-4}$ S $m^{-1}$ (conductivity), $\pm 2 \times 10^{-3}$ °C (temperature) and of the dissolved oxygen sensor less than 8 μmol $L^{-1}$. The chlorophyll *a* fluorescence sensor has a sensitivity of $1.6 \times 10^{-2}$μg $L^{-1}$ and the CDOM of 0.184 ppb.

The AUV profiled down to 100 m and made a total of 38 dives (76 profiles). The temperature, salinity, and dissolved oxygen from the AUV were compared to the ship's CTD sensors. No correction was necessary for salinity or temperature, but an offset of 40 μmol $kg^{-1}$ was applied to the dissolved oxygen concentration. In this study, we use the apparent oxygen utilization (AOU, in μmol $kg^{-1}$): AOU = $[O_2] - S_{O_2}$ where $S_{O_2}$ is the solubility of the dissolved oxygen at a given temperature. Variations in AOU are independent of the variations in temperature.

### 2.3. Current Measurements

*R/V Kronprins Haakon* was equipped with four SADCPs, two 38 kHz RDI Ocean Surveyors and two 150 kHz RDI Ocean Surveyors, a pair on a drop keel at 3.4 m depth, and a pair in the hull for protected measurements in sea ice. For the purpose of this study that focuses in the upper ocean in open water, we only used data from the 150 kHz SADCP installed on the drop keel. The SADCP continuously collected velocity profiles (every 5 min), in 65 bins of 8 m vertical thickness after a 6 m blank distance. Final postprocessing of the SADCP profiles was done by using the CODAS package (maintained at https://currents.soest.hawaii.edu). Typical processed horizontal velocity uncertainty is 2-3 cm $s^{-1}$.

### 2.4. Thermosalinograph Data

Near-surface temperature and salinity measurements were made continuously every 10 s using a SBE thermosalinograph. The water intake depth was 4 m. The salinity was out of range and not used, but the surface temperatures were accurate after applying an offset of 0.5 °C (Figure 2c, red line), determined after comparing against the ship's CTD.

### 2.5. Other Data Sets

The profiles collected from the ship's CTD system (SBE 911plus) are used to check and correct the temperature (AUV, thermosalinograph, and VMP), salinity (AUV and VMP), and dissolved oxygen (AUV) data.

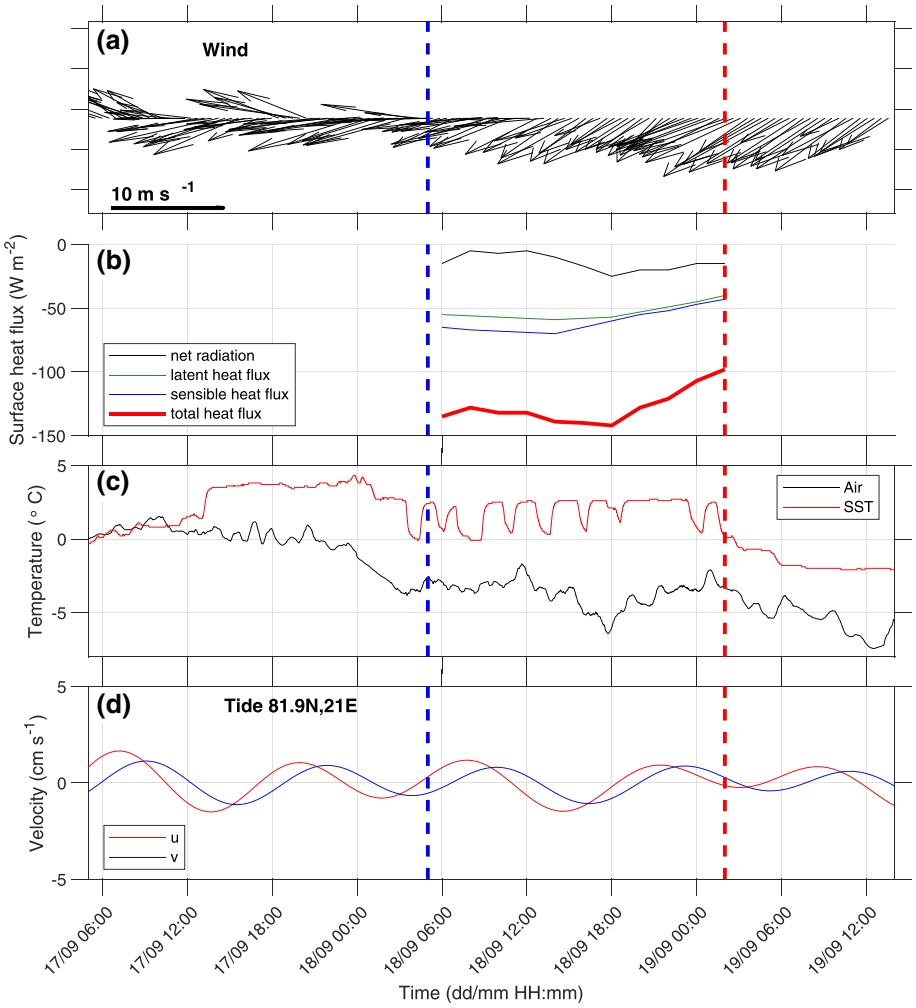


**Figure 2.** Times series of (a) wind vectors measured from the weather mast on *R/V Kronprins Haakon*; (b) net surface heat flux (red line), with components of net radiation (measured, in black) and sensible (from model, in blue) and latent heat fluxes (from model, in green); (c) air temperature (black) from the weather mast and sea surface temperature (red) from the thermosalinograph; and (d) tidal currents (east, $u$, and north, $v$, components) from the AOTIM-5 barotropic tide model. The blue/red vertical dashed line indicates, respectively, the beginning/end of the front study.

CTD data were processed using the standard software, SBEDataProcessing-Win32, and salinity and oxygen values were corrected against water sample analyses.

The wind speed, direction, and surface air temperature (Figures 2a and 2c) were recorded every minute during the cruise from the ship's weather station. Outside the cruise dates, the ERA5 reanalysis is used (www.ecmwf.int/en/forecasts/datasets/reanalysis-datasets/era5).

Total net surface flux Q (in W m$^{-2}$, positive downward into the ocean, Figure 2b) is expressed as $Q = Q_{rad} + Q_l + Q_s$, with $Q_{rad}$ the net radiation (sum of net shortwave and longwave radiation), $Q_l$ the latent heat flux, and $Q_s$ the sensible heat flux. $Q_{rad}$ was measured on board using a Kipp & Zonen CNR 4 surface net radiometer (M. Müller, personal communication, 2019), while $Q_l$ and $Q_s$ are obtained from the AROME model (Müller et al., 2017). As the sensible heat flux is proportional to the difference of temperature between the surface air temperature and the sea surface temperature, variations of the surface temperature across the front have been taken into account in the AROME estimates of the sensible heat flux by rescaling it with the measured surface temperature. In the latent heat flux, we neglect the influence of variations of the surface temperature, which is less than 4 W m$^{-2}$ around the Svalbard region (Kumar et al., 2017).

The barotropic tide (Figure 2d) is estimated at the front location using the AOTIM-5 model (Arctic Ocean tidal inverse model) (Padman & Erofeeva, 2004). We used the updated version in 2018, which estimates the eight main components ($M_2$, $S_2$, $N_2$, $K_2$, $K_1$, $O_1$, $P_1$, and $Q_1$) and four nonlinear components ($M_4$, $MS_4$, $MN_2$, and $2N_2$) on a 5 km horizontal resolution grid.

For context, temperature and salinity profiles collected by a Seaglider are also used. The glider was deployed during the cruise and was recovered in the beginning of November, north of Svalbard. The data were processed using the University of East Anglia Seaglider toolbox (http://www.byqueste.com/toolbox.html), based on the methods described by Garau et al. (2011) and Frajka-Williams et al. (2011). Processed salinity and temperature data are accurate to $1 \times 10^{-2}$ g kg$^{-1}$ and $1 \times 10^{-3}$ °C, respectively. Data spikes above three standard deviations were removed during postprocessing.

The sea surface temperature map is based on the observations from the satellite Metop$_A$ AVHRR instrument, downloaded from Copernicus marine environment monitoring service (http://marine.copernicus.eu/). The product is a daily interpolated field with a 0.05° resolution and covers surface temperatures in the ocean, the sea ice, and the marginal ice zone.

## 3. Environmental Context

The near-surface front was located around 81.9°N, 21°E, in the Nansen Basin (bottom depth of 3,400 m) at the exit of the Sofia Deep (Figure 1a). The physical oceanography and mixing processes in this region have been extensively documented from January to June 2015 during the Norwegian young sea ICE expedition (N-ICE2015) (Meyer, Fer, et al., 2017; Meyer, Sundfjord, et al., 2017). In this region, turbulence is mainly driven by wind and by tidal currents over slopes. Turbulent heat fluxes exceeding 100 W m$^{-2}$ were observed during strong wind episodes and when Atlantic Water was close to the pynocline, leading to rapid sea ice basal melt (Meyer, Fer, et al., 2017). This region typically hosts the marginal ice zone, as during our observations in September 2018.

During our measurements, sea ice edge was visible from the ship, and a Sentinel 1 image confirms that the front was located 4–5 km from the sea ice edge (Figure 1a). The average wind speed was moderate with 7 m s$^{-1}$ from northeast, and the tidal currents were weak, less than 3 cm s$^{-1}$ (Figures 2a and 2d). The external mechanical forcing was thus not energetic and relatively constant, with negligible time variability throughout the front survey (Figure 2).

During the front survey, air temperature was around −4 °C on average, and the sea surface temperature oscillated between 0 and 4 °C (Figure 2c). After the front study was completed on 19 September 2018, the vessel headed farther north into the sea ice in the Nansen Basin, the air temperature and the surface ocean temperature dropped, respectively, to −5 °C and to −1.8 °C, the ocean freezing temperature. At the front location, the net surface heat flux was destabilizing, varying between −140 and −180 W m$^{-2}$ (Figure 2b), with $Q_{rad} \sim -15$ W m$^{-2}$, $Q_l \sim -55$ W m$^{-2}$, and $Q_s \sim -64$ W m$^{-2}$ (Figure 2b). Fumes over the surface ocean were photographed on 18 September 2019, confirming visually the large sensible and latent heat fluxes (M. Müller, personal communication, 2019).

Based on ship's CTD profiles collected only down to 500 m at the front study, the Rossby radius of deformation, $R_D = c/f$, was 3 km ($f$ is the Coriolis parameter) when calculated using the first baroclinic phase speed, $c$, from the stratification measured in the upper 500 m, or 10 km when the deepest measurement was extrapolated to full depth. The mixed layer deformation radius, defined as $R_{ml} = ND_{ml}/f$ where $D_{ml}$ is the mixed layer depth, varied in the range of 1 and 4 km.

## 4. Methods

### 4.1. Determination of the Surface Front Location

The location of the surface front was identified using all available near-surface temperature observations (Figure 1b). The uppermost depth sampled by each instrument is used: 4 m from the thermosalinograph, 6 m from the VMP, and 2 m from the AUV. These measurement depths are within the mixed layer and are representative of the surface temperature. The data set was collected within 26 hr, and therefore, advection cannot be neglected. Assuming negligible change in the water mass properties during the measurements, we construct a synoptic data set by advecting the sample locations to a common time, 18 September 2018 at 12:00 UTC.

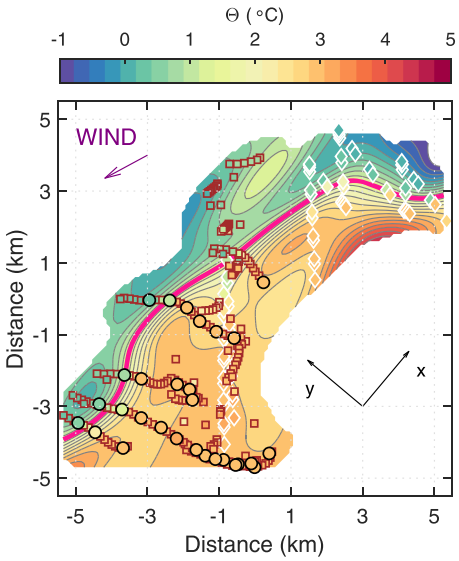


**Figure 3.** Near-surface temperature distribution obtained by objective mapping of the measurements near the front location. Only regions with an objective interpolation error less than 10% are shown. The measurement locations have been advected to a common time of 18 September 2018, 12:00 UTC. The surface temperature data are from VMP (circles), thermosalinograph (squares), and AUV (diamonds). Note the AUV path autonomously crossing the front. The pink contour is the 1.5 °C isotherm, chosen to represent the front location. The coordinate system shows the along-front ($x$) and cross-front ($y$) directions. The purple arrow is the mean wind direction during the process study (average amplitude of 7 m $s^{-1}$).

The stations were relocated by advecting the analyzed water column (upper 100 m) with the observed velocity at 25 m depth (the uppermost bin of the SADCP), after smoothing with a 1-hr running mean to remove the small-scale and local variations. This is considered representative of the surface currents in the region. The current velocities showed vertical variability but typically less than 20 cm $s^{-1}$. The approximation of uniform current in the upper 100 m introduced negligible error and differential advection in the depth range and duration of the station. A sensitivity test by mapping the surface temperature using the speed measured at 50 or 90 m gave similar results (not shown).

The adjusted station locations are shown in Figure 3. The near-surface temperature is then mapped using an objective interpolation. As the vessel crossed the front, the thermosalinograph captured the strong surface temperature change (Figure 2c). The location of the front was well represented by the 1.5 °C isotherm (our results are not sensitive to an alternative definition using 2 or 1 °C). The front was oriented in the southwest-northeast direction, with the cold and lighter side toward the northeast (Figure 3). The horizontal decorrelation length scales used in the objective interpolation are estimated as 3 km in the along-front direction and 1 km in the cross-front direction, from the zero crossing of the autocorrelation of detrended surface temperatures ordered in ascending longitude or latitude, respectively.

### 4.2. Construction of a Front Section

Cross-front sections of hydrography, currents, and turbulence were constructed after assigning a cross-front distance to each measurement point, defined as the distance closest to the front (positive on the cold side) after relocating (advecting) each station to 12:00 UTC as shown in Figure 3. The cross-front sections are obtained after a series of objective interpolations (Figure 4). First, the stations are advected and objectively mapped horizontally every 1 m depth to remove small scale variability. Along-front decorrelation length scale is 3 km, comparable to the mixed layer deformation radius, whereas the cross-front decorrelation length scale is 1 km. The mapped profile at each station location is then extracted to reconstruct distance-to-front sections. This new field with scattered horizontal distance is once again objectively mapped on the horizontal and vertical (cross-front decorrelation length scale of 1 km and vertical decorrelation length scale of 20 m, Figure 4) to obtain a gridded distance-depth field. Note that depending on the parameter shown, the sampling is biased to the warm side (VMP, blue triangles in Figure 4) or the cold side (AUV, red triangles in Figure 4).

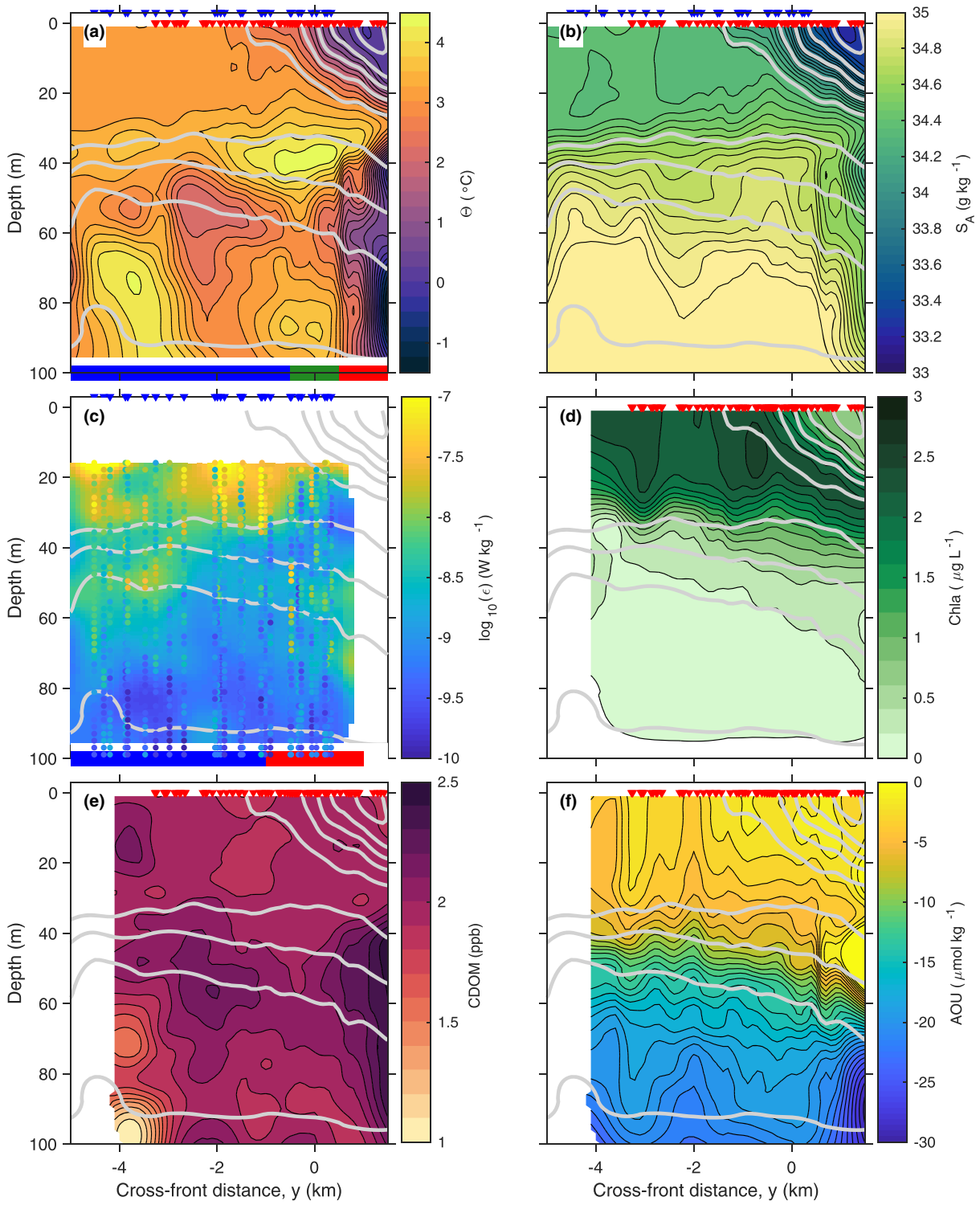


**Figure 4.** Composite cross-front sections of (a) conservative temperature (Θ), (b) absolute salinity ($S_A$), (c) dissipation rate ($\epsilon$), (d) chlorophyll *a* fluorescence, (e) CDOM (ppb), and (f) apparent oxygen utilization (AOU). The red/blue triangles are the location of the AUV/VMP profiles, respectively. The gray lines are isopycnals (every 0.1 kg m$^{-3}$). In panel c, the color-coded dots correspond to the in situ observations collected with the VMP. In panels a and c, the blue, green, and red lines indicate the cross-front ranges used to create the averaged profiles in Figure 6 (colorcode in panel a) and Figure 7 (colorcode in panel c).

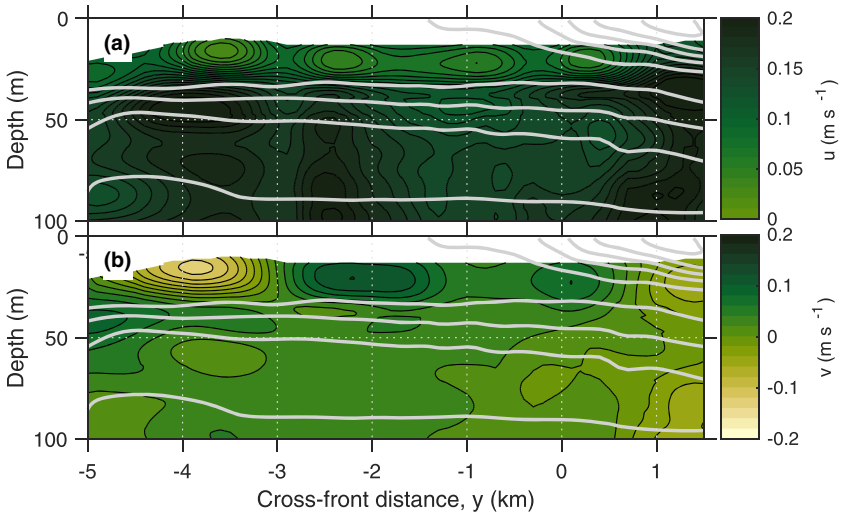


**Figure 5.** Cross-front sections of the velocity components (a) along the front ($u$) and (b) across the front ($v$). The gray lines are isopycnals (every 0.1 kg m$^{-3}$).

For the current velocities, along ($u$) and cross-front ($v$) components are defined using the mean front orientation in the region where the ship observations were made (Figure 3, oriented along a mean angle of 50° from the East). The gridded sections are then obtained similar to the other parameters (Figure 5). Note that the front orientation is different at the AUV site; however, the decomposition into along and cross-front components is only used for the velocities measured by the SADCP.

### 4.3. Summary of Depth Ranges Used in Calculations

Our analyses are based on different parameters and depth ranges depending on the processes discussed. Here we present a brief summary of the relevant choices made. All AUV data (temperature, salinity, AOU, CDOM, and chlorophyll a fluorescence) are 1-m vertical averages, collected in the 2–90 m depth range and are objectively mapped, filling the gap to the surface. Temperature and salinity profiles from the VMP are 2-m vertically averaged and objectively mapped. Dissipation measurements are available below 15 m depth. The uppermost measurement is extended to the surface for calculation of depth-integrated dissipation rates. SADCP horizontal currents are at 8 m vertical resolution starting from 25 m depth. The uppermost measurement is extended to the surface. This uppermost measurement is used to advect the station locations.

The forced symmetric instability (FSI, subsection 6.2) is active down to 40 m. The Ekman Buoyancy Flux (EBF, defined in equation (9)), which fuels the FSI, is a process driven by Ekman fluxes in the surface layer; hence, it is calculated as the average in the top 20 m. In the analysis, to be consistent with EBF and to account for variations near the surface, potential vorticity (defined in equations (5) to (8)) is averaged in the upper 20 m (Figures 8a and 9a).

## 5. Observations

### 5.1. Hydrography and Currents

The surface front is visible in the sections of temperature, salinity, and chlorophyll $a$ fluorescence (Figures 4a, 4b, and 4d). At the front, the near-surface cross-front temperature gradient was −0.9 °C km$^{-1}$, and the salinity gradient was −0.35 g·kg$^{-1}$·km$^{-1}$. Temperature and salinity gradients were not compensated, and the associated surface cross-front density gradient was −0.21 kg·m$^{-3}$·km$^{-1}$. On the cold side ($y > 0$), the surface layer was composed of Polar Surface Water ($\sigma_0 < 27.70$ kg m$^{-3}$; Rudels et al. (2000) and Figure 6), while on the warm side the mixed layer was deeper and denser. For each profile, the mixed layer depth was calculated as the depth where the density at the surface increased by 10% of the difference between the surface density and the density at 100 m. It was about 30 m on the warm side and decreased from 15 m at the front to about 10 m on the cold side.

The surface temperature front extended down to about 30 m, which is the depth of the mixed layer on the warm side. The chlorophyll $a$ fluorescence cross-front section (Figure 4d) shows higher concentration in

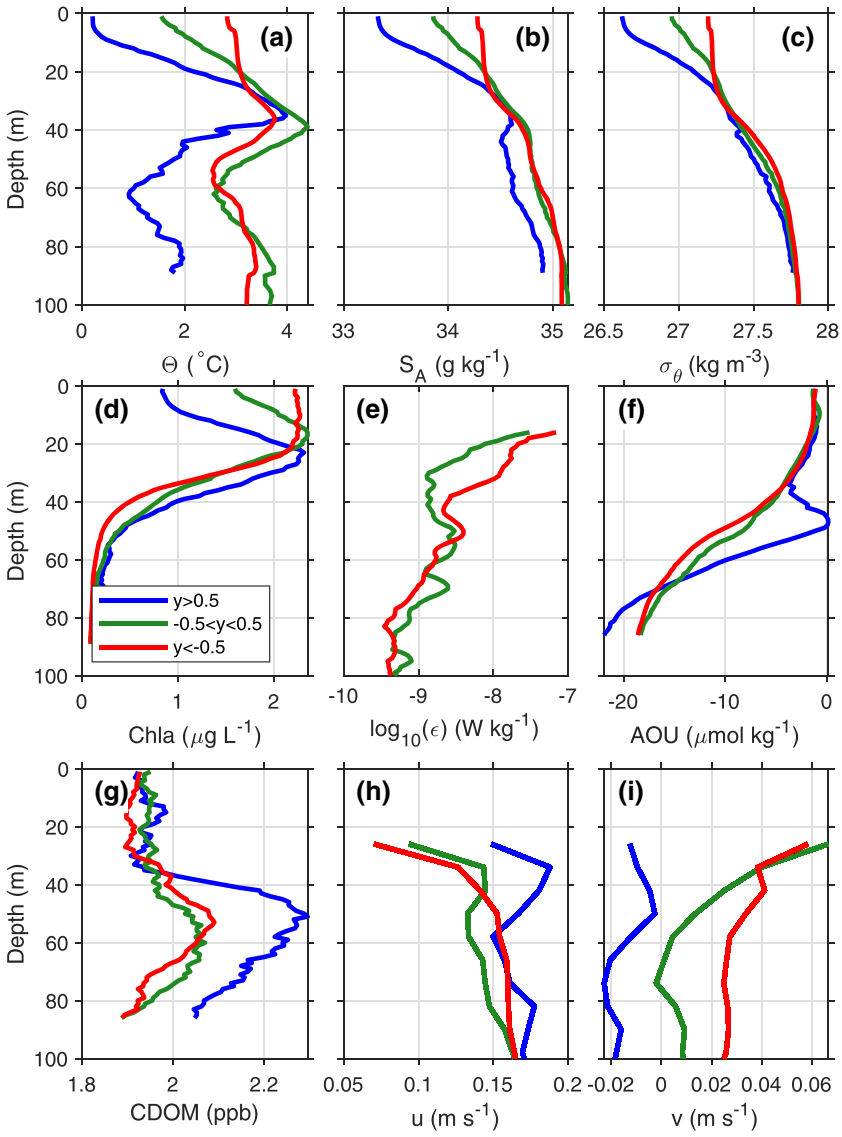


**Figure 6.** Averaged profiles in cross-front distance ranges. (a) Θ), (b) $S_A$, (c) $\sigma_\theta$, (d) chlorophyll *a* fluorescence, (e) $\epsilon$, (f) AOU, (g) CDOM, (h) along front velocity ($u$), and (i) cross-front velocity ($v$). In blue: average of the profiles located on the cold side with $y > 0.5$ km. In green: average of the profiles located within 0.5 km of the front. In red: average of the profiles located on the warm side with $y < -0.5$ km.

the mixed layer on the warm side compared to the mixed layer on the cold side (2.5 μg $L^{-1}$ compared to 0.8 μg $L^{-1}$, respectively). At the front location ($-0.5 < y < 0.5$ km), chlorophyll *a* fluorescence was elevated between 20 and 30 m, associated with a ~10 m deepening of the isopycnals (Figures 6c and 6d).

There is no current measurements in the upper part of the mixed layer as the SADCP only sampled deeper than 25 m. Observations slightly shallower than 25 m visible in Figure 5 are from the objective mapping. The along and cross-front velocity components show some differences in the deeper part of the mixed layer (~25 m), with a shear in the across velocity: Warm waters move toward the cold side and the cold waters toward the warm one (Figure 5). The differences in velocities are more distinct when presented as average profiles in different cross-front distance ranges (Figures 6h and 6i). The current velocities suggest the downwelling of the "warm" mixed layer under the "cold" mixed layer. This process explains the large concentration of chlorophyll *a* fluorescence at 30 m depth (~2.5 μg $L^{-1}$, concentrations similar to the one found in the warm mixed layer) under a layer rather depleted in chlorophyll *a* fluorescence (the cold mixed layer) (Figures 4d and 6d).

Temperature section (Figure 4a) shows several layers: a surface layer down to 30 m with a strong surface temperature and salinity front and a warm layer at about 35 m above a cold layer at about 55 m. Averaged profiles are calculated with respect to distance to front, cold or warm side ($|y| > 500$ m), or at the front ($|y| < 500$ m). We use warm (red) and cold (blue) color for the respective side of the front, and green at the front, for easy visual orientation. At about 35 m depth, the warm layer had temperatures of 4–4.5 °C, above a cold intrusion (1–3 °C) at about 55 m depth. The warm intrusion was warmer at the front location (~4.3 °C, Figure 6a) than on the warm side (~3.8 °C). Analyzing observations from a larger scale (250 km cross-front and 300 m vertical extents) thermohaline front north of Svalbard, May and Kelley (2001) suggested that intrusions developed from double-diffusive interleaving and were maintained by diffusive convection fluxes. Our analysis using cross-front intrusion slope and along-intrusion density ratio following the methods of May and Kelley (2001) remains inconclusive (not shown) on the role of double diffusion in shaping the intrusions. We hypothesize that the intrusions are caused by the local dynamics and the induced secondary circulation at the front (see subsection 7.1 for more details).

The surface front was colocated with a subsurface front below the mixed layer. Temperatures on the cold/warm side of the front at 60 m depth were about 1.3/3.0 °C, respectively, with corresponding salinities of about 34.6/35 g kg$^{-1}$ (Figure 6). The water at depth on the warm side is of Atlantic origin and was probably advected from the slope north of Svalbard. Values of CDOM and AOU were fairly homogeneous and did not show strong lateral gradients at the surface front but showed differences at depth. Between 40 and 100 m depth on the cold side, the water mass was enriched in CDOM (2.3 vs. 2 ppb, respectively), which characterizes Polar Water compared to water masses coming from Fram Strait (Athanase et al., 2019). The AOU was null at the surface. The front location was free of ice, and the surface layer was at equilibrium with the atmosphere, hence saturated in oxygen. The AOU profile on the cold side shows a distinct subsurface increase in concentration, reaching 0 at about 40 m (Figure 6f). This patch of water, which has recently been in contact with the surface, can be associated with the subduction of the warm mixed layer beneath the cold side, below the waters less saturated in oxygen (see subsection 7.1 for more details). At depth (~80 m), the AOU was lower on the cold side (approximately −23 μmol kg$^{-1}$ compared to approximately −18 μmol kg$^{-1}$ on the warm side, Figure 6). Waters at depth (70–100 m) on the cold side have been isolated from the surface for a longer time than those on the warm side. Based on the temperature, salinity, CDOM, and AOU characteristics, we infer that the water at depth on the cold side of the front is modified Atlantic Water that has already recirculated in the Arctic: These waters come from the deep Nansen Basin.

### 5.2. Turbulence

Dissipation measurements were concentrated on the warm side and at the front location. Dissipation rate was largest in the upper 30 m (Figures 4c and 6e), reaching $10^{-7}$ W kg$^{-1}$ and decreasing to $3 \times 10^{-10}$ W kg$^{-1}$ at 90 m. Down to ~30 m, the dissipation rate on the warm side was larger by 1 order of magnitude compared to the front location (Figure 6e). Possible sources for the observed turbulence in the upper layers resolved by our measurements are discussed in the next section. Deeper patches of turbulent water ($\epsilon = 5 \times 10^{-9}$ W kg$^{-1}$) were also detected, for example, at around 50 m depth between −3 and −4 km and on the cold side between 50 and 70 m depth (Figure 4c). One possible source of turbulence in the stratified layer below the mixed layer is the shear instability; however, the vertical resolution of our current measurements (8 m) is not sufficient to investigate this mechanism. At the front location around $y = 0$ km, moderate dissipation rates (about $10^{-9}$ W kg$^{-1}$) were observed down to 40 m, two to three times deeper than the mixed layer depth. The next section focuses on the possible sources of turbulence in the upper layer, at the front location and on the warm side. In the following analyses, we use the individual dissipation rate profiles, not the objectively mapped field (Figure 6).

## 6. Sources for Turbulence

### 6.1. Convection and Wind Stress

The net loss of heat to the atmosphere led to destablizing buoyancy fluxes during the study period. While wind forcing was moderate, its contribution to the turbulent kinetic energy production in the upper ocean cannot be neglected. The scaling suggested by Lombardo and Gregg (1989) considers the contribution of both convection and wind stress in the form of $\epsilon = 0.58B_0 + 1.78\epsilon_s$, where $B_0$ is the surface buoyancy flux (positive is destabilizing) and $\epsilon_s$ is the stress scaling for a wall layer. These parameters are calculated using $B_0 = -\frac{g\alpha Q}{\rho_0 C_p}$, where $\alpha$ is the thermal expansion coefficient of about $10^{-4}$ K$^{-1}$ and $Q$ is the net surface heat flux, and $\epsilon_s = \frac{{u_*}^3}{\kappa z}$, where the friction velocity $u_*$ is obtained from the wind stress magnitude using a

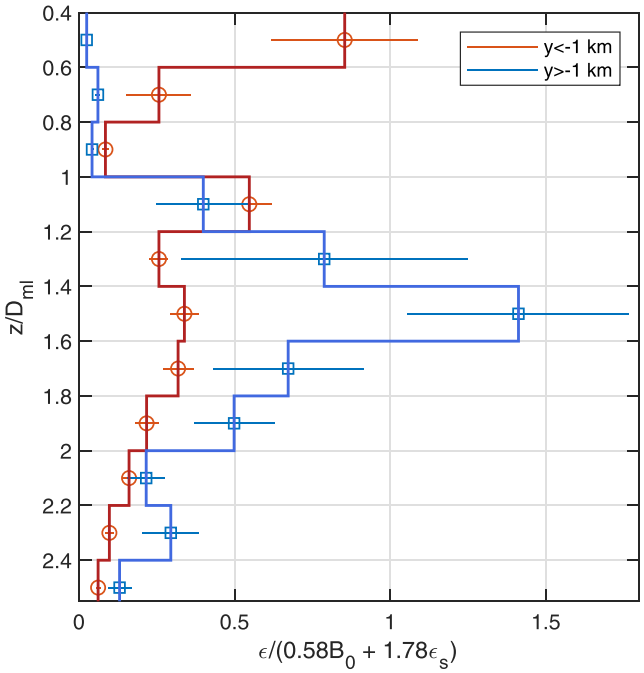


**Figure 7.** Mean profiles of dissipation rate scaled by the contribution of wind stress and of convection (Lombardo & Gregg, 1989), averaged near the front (blue) and on the warm side (red). The vertical axis is depth normalized by the mixed layer depth, $D_{ml}$. Vertical averaging is over $z/D_{ml} = 0.2$ thick bins. The horizontal bars are the standard error.

drag coefficient of $2.7 \times 10^{-3}$ and $\kappa = 0.4$ is the von Karman constant. Individual dissipation profiles are vertically scaled with the mixed layer depth, $D_{ml}$ obtained from the corresponding potential density profiles, and bin-averaged in 0.2-thick bins of $z/D_{ml}$ (Figure 7). Two profiles are shown, one for the warm side (red) and one near the front (blue). The cold side is undersampled by the VMP, both in terms of number of profiles and also in resolving the vertical extent of the shallow mixed layer (dissipation data are reliable only below 15 m depth; section 2).

Close to the surface in the mixed layer and on the warm side with relatively deep mixed layer, the scaled dissipation is close to 1; hence, convection and wind forcing can account for the turbulence rate observed near the surface. At the front location, the mixed layer turbulence is much more quiescent than that predicted by the scaling. In the shallow mixed layer overlaying the strong vertical stratification, we might expect buoyancy effects suppressing turbulence in the lower part of the normalized depth (note that our data cover only $z/D_{ml} > 0.4$). Our profiles do not resolve the turbulence structure for mixed layer depth less than 15–20 m, and the quiescent profiles relative to the scaling can be biased by our limited data set. However, below the mixed layer, observed dissipation is more energetic than the scaling, with a maximum reaching a scaled dissipation of 1.4 at about 1.5 mixed layer depth. At the front location, the increased dissipation rates below the mixed layer require an additional source of energy.

### 6.2. Possible Contribution From Forced Symmetric Instability

Symmetric instability develops in weakly stratified waters when the horizontal buoyancy gradient and vertical shear of a geostrophic current act to reduce the potential vorticity ($q$) to take the opposite sign of the Coriolis parameter, $f$ (i.e., $fq < 0$). Turbulence is generated with energy drawn from the kinetic energy of the balanced flow. Background eventually adjusts to a state of marginal stability with $q = 0$ (Thomas et al., 2013). Forced symmetric instability (FSI) occurs, however, sustaining turbulence for extended periods, when down-front winds or destabilizing convection induce diabatic potential vorticity fluxes to maintain $fq < 0$. Energy transfer to dissipation occurs through secondary Kelvin-Helmholtz instabilities following symmetric instability (Taylor & Ferrari, 2009).

A symmetrically unstable flow is characterized by a geostrophic potential vorticity ($q_g$) of the opposite sign of the Coriolis parameter, $f$, (i.e., $q_g < 0$ in the Northern Hemisphere), absolute vorticity ($f + \zeta$) of the same sign of the Coriolis parameter ($f + \zeta > 0$ in the Northern Hemisphere), and stable stratification ($N^2 > 0$)

(Thomas et al., 2013, 2016). Assuming that the flow does not vary in the along front direction and following Thomas et al. (2016), relative vorticity is approximated by

$$\zeta = -\frac{\partial u}{\partial y}. \tag{4}$$

Rossby number, $\mathrm{Ro} = \zeta/f$, was anticyclonic ($< 0$) on the cold/light side, reaching $-0.8$ at $y = 0.7$ km (vertical average in the upper 30 m), and highly variable on the dense side, varying between $-0.3$ and 0.5, with an average of 0.05. Values of Ro near unity in the cold side suggest that submesoscale and nonlinear processes can be important. The potential vorticity $q$ can be expressed as two terms emphasizing the role of the vertical vorticity/stratification, $q_{vert}$, and the baroclinicity, $q_{bc}$.

$$q = q_{vert} + q_{bc} \quad , \tag{5}$$

with

$$q_{vert} = (f + \zeta)N^2, \tag{6}$$

$$q_{bc} = \frac{\partial u}{\partial z}\frac{\partial b}{\partial y}. \tag{7}$$

$N^2$ is the Brunt-Väisälä frequency, $u$ is the along-front velocity, and $b$ is the buoyancy ($b = -\frac{g}{\rho_0}\sigma_0$). The geostrophic potential vorticity $q_g$ is approximated by

$$q_g = (f + \zeta)N^2 - \frac{1}{f}\left(\frac{\partial b}{\partial y}\right)^2, \tag{8}$$

where the geostrophic shear is substituted as $\frac{\partial u_g}{\partial z} = -\frac{1}{f}\frac{\partial b}{\partial y}$.

Potential vorticity near the surface can be reduced by Ekman dynamics in favorable conditions. The Ekman buoyancy flux (EBF) is the product of the Ekman transport and horizontal surface buoyancy gradient and quantifies the buoyancy flux induced by Ekman advection and density gradient across the front:

$$\mathrm{EBF} = -\frac{\tau_x}{\rho_0 f}\frac{\partial b_s}{\partial y}, \tag{9}$$

with $\tau_x$ the along-front component of the wind stress and $b_s$ the near-surface buoyancy. For down-front wind stress, the EBF becomes positive, and dense surface water is advected over lighter water and tends to destabilize the stratification resulting in a reduced potential vorticity. Using the weather data from ship (Figure 2), we calculated $\tau_x$. Potential vorticity components and EBF are presented in Figure 8. On the warm side of the surface front, the EBF and the upper 20-m depth-averaged potential vorticity are negligible. At the front location in the upper 30 m, the geostrophic potential vorticity is negative (Figure 8b) while the EBF becomes positive. As $q_{vert} > 0$, $q_g < 0$ is due to the second term of equation (8). The EBF tends to reduce the potential vorticity in the boundary layer (Figure 8a). At the front location, in the upper 20 m, $q$ and $q_g$ are of opposite sign, an indication of strong ageostrophic shear.

The depth of the low potential vorticity layer (or surface boundary layer), $H$, was estimated following Thomas et al. (2013) (Figure 8c, black line), as the depth where the balanced bulk Richardson number, $\mathrm{Ri}_{\mathrm{bulk}} = \frac{H\Delta b}{(\Delta u_g)^2} = 1$ at $z = -H$. Here, $\Delta$ is the change in a value from the surface to $z = -H$. The depth of the convective layer, $h$, is obtained from the scaling given in Taylor and Ferrari (2010), solving the nonlinear equation 24 of Thomas et al. (2013) for each $H$ and neglecting entrainment terms (Figure 8c, red line). At the front location, the convective layer depth, $h$, is very shallow and $H \sim 35 - 40$ m, while on the warm side $h$ is about 20 m, and $H$ is about 25 m (Figure 8c).

Depth-integrated dissipation, $D = \rho_0 \int \epsilon dz$, is calculated by integrating over the upper 100 m as well as over $H$. In each case, the missing data at the surface are filled in by extrapolating the uppermost measurement. When integrated over $H$, $D$ accounts for almost the entire dissipation in the upper 100 m, especially at the front location, with values exceeding $3 \times 10^{-3}$ W m$^{-2}$ (Figure 9b). These are associated with vertically averaged turbulent heat fluxes of up to 10 W m$^{-2}$ (Figure 9c). Following Thomas and Taylor (2010), the net total

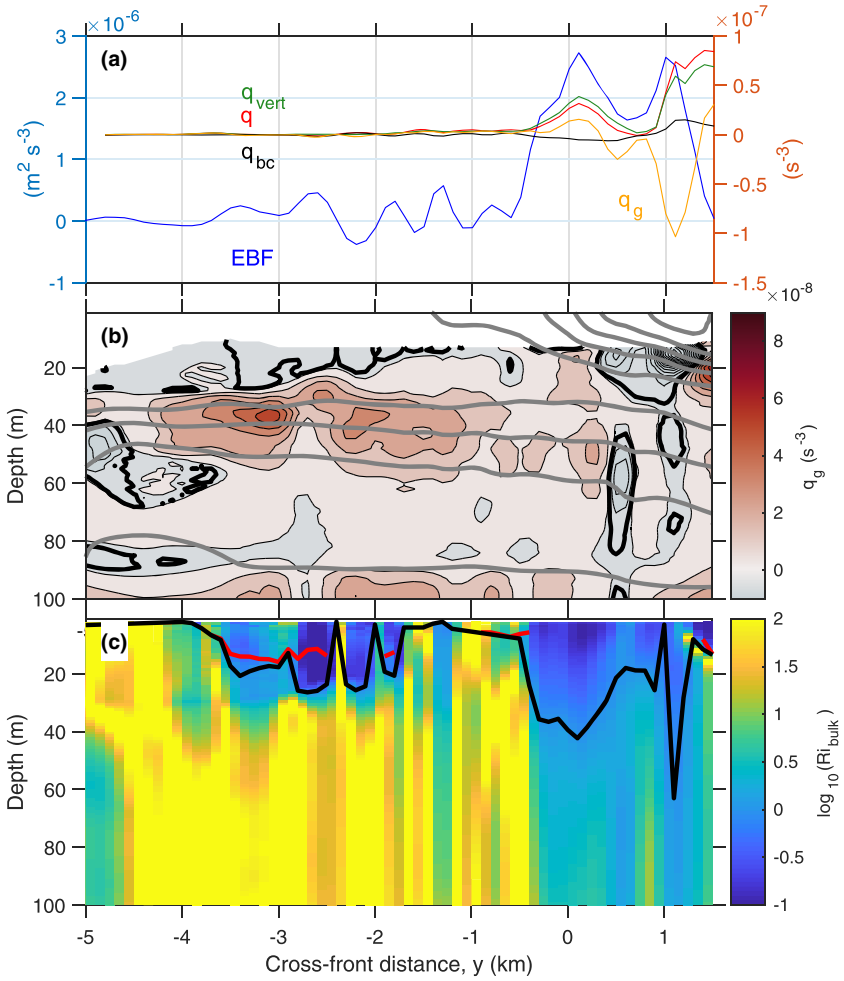


**Figure 8.** (a) Cross-front distribution of Ekman buoyancy flux (EBF, blue, left axis), upper 20 m depth-averaged potential vorticity terms (right axis), total $q$ (red), its vertical component (green), its baroclinic component (black), and the geostrophic potential vorticity (orange). Depth-cross-front distance distribution of (b) geostrophic potential vorticity and (c) bulk Richardson number. In (b) gray contours are isopycnals and the black contour is $q_g = 0$. The black line in (c) is the low PV layer depth $H$, corresponding to $Ri_{bulk} = 1$, and the red line is the convective layer depth $h$.

dissipation from FSI can be expressed as $D_{EBF} = \rho_0 \int \epsilon_{SI} dz = \rho_0 \times H \times \mathrm{EBF}/2$ (Figure 9, blue squares). This assumes that the dissipation rate generated by FSI, $\epsilon_{SI}$, decreases linearly from its surface value to 0 at $H$, a profile shape supported by their large eddy simulation analyses. At the front location, $D_{EBF} \sim 3.0 \times 10^{-2}$ W m$^{-2}$, and on the warm side about $10^{-3}$ W m$^{-2}$.

Our calculations show that the front is susceptible to develop FSI; however, the observed dissipation integrated over $H$ is lower than the potential supply from FSI (Figure 9b). We do not observe a substantial increase in dissipation rates driven by FSI at the front location. There is no conclusive evidence; however, the turbulence production by FSI could potentially contribute to the elevated dissipation rates beneath the mixed layer (Figure 7, blue profile).

## 7. Discussion

### 7.1. Vertical Circulation

Large vertical velocities can develop at fronts and affect the distribution of properties such as the chlorophyll a fluorescence. For example, biogeochemical fluxes can be driven by ageostrophic cross-frontal circulations associated with a meandering of a density front (Pollard & Regier, 1992). Down-front wind can intensify the ageostrophic cross-frontal circulation through nonlinear Ekman pumping (Lee et al., 1994). The horizontal deformation of a front thus can play an important role in driving vertical velocities. We estimated the vertical

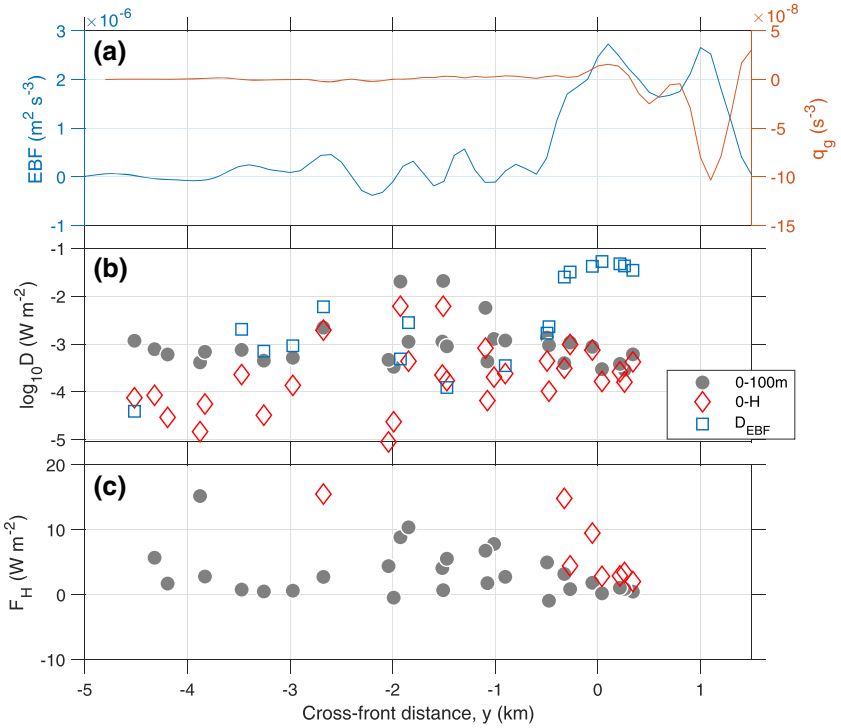


**Figure 9.** (a) Ekman buoyancy flux, EBF, (left axis in blue) and the geostrophic component of the potential vorticity ($q_g$) averaged over the upper 20 m (right axis). (b) Depth-integrated dissipation rate, $D$, integrated over the upper 100 m (gray dots), over the low PV layer depth, $H$ (red diamonds), and from forced symmetric instability over $H$ (blue squares). (c) Turbulent heat flux averaged over the upper 100 m (gray dots) and over H (red diamonds).

velocity $w$ using the quasi-geostrophic $\omega$ equation (Hoskins et al., 1978):

$$N^2\nabla_h^2 w + f^2\frac{\partial^2}{\partial^2 z}w = 2\nabla.\mathbf{Q}, \tag{10}$$

where $\mathbf{Q}$ is the divergence of the kinematic deformation: $\mathbf{Q} = \nabla\mathbf{u}.\nabla\frac{g\rho}{\rho_0}$. We obtained $\mathbf{Q}$ using the objectively interpolated composite cross-front sections (density and cross-front velocity component are shown in Figure 5b). A 10 m and 1,000 m running mean was applied vertically and horizontally, respectively, because the vertical velocities are sensitive to noise through the second derivatives involved in $Q$. The boundary condition is set to $w = 0$ on all edges of the domain; the solution near the side and bottom boundaries (at 100 m depth) should therefore be interpreted with caution, and we only show the central part of the domain in Figure 10.

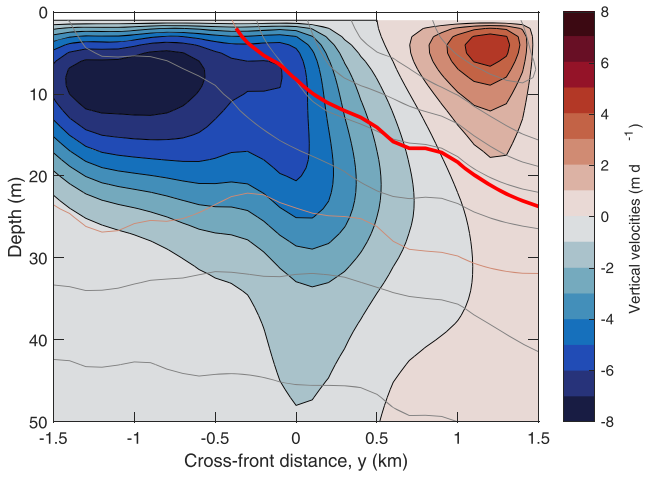


**Figure 10.** Cross-front vertical velocities inferred from the $\omega$-equation. Velocities are negative downward and positive upward. The red line is the 2 μg $L^{-1}$ Chlorophyll a fluorescence concentration (from Figure 4d). Gray lines are isopycnals.

The vertical velocities computed in the cross-front section are shown in Figure 10 together with isopycnals and a selected chlorophyll a fluorescence concentration contour. This contour is representative of the distinct downwelling signature detected in the chlorophyll a fluorescence distribution measured by the AUV. On the warm, dense side of the front, we infer negative, downward velocities extending to the front location (Figure 10), reaching a maximum of 8 m $day^{-1}$. On the light, cold side of the front, upward velocities exceed 4 m $day^{-1}$. The vertical circulation documented here is consistent with a thermally direct circulation (i.e., restratifying) expected from the converging cross-slope velocity at the front and is similar to the circulation patterns reported in Johnston et al. (2011) and in Thomas and Joyce (2010). These velocities could drive the vertical fluxes leading to the deepening of chlorophyll a fluorescence maximum under the cold mixed layer (Figure 10, red line). The vertical

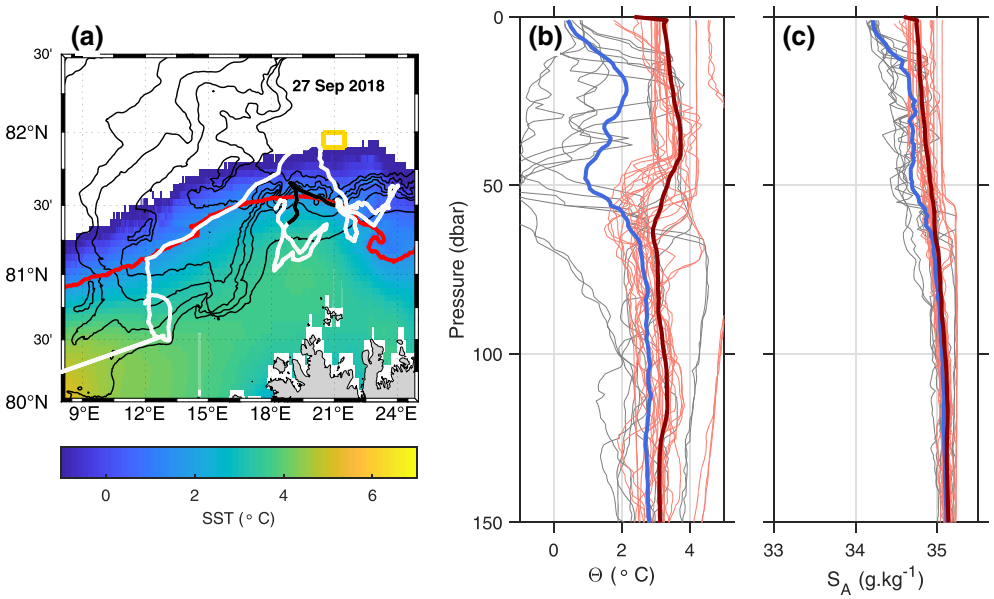


**Figure 11.** (a) Seaglider trajectory (white) together with sea surface temperature map (SST) for 29 September 2018 and isobaths. The absence of data indicates the presence of sea ice. The 1.5 °C contour (red) marks a front. The black trajectory highlights the crossing of the front. Profiles of (b) Θ and (c) $S_A$ obtained along the black trajectory. Cold colors (gray and blue) are profiles from the cold side of the front, and the warm color from the warm side. The thick curves are the average profiles for the cold (blue) and warm (red) side.

velocities might also explain the formation of the cold and warm intrusions at, respectively, 45 and 35 m depth and are consistent with the subsurface patch of water on the cold side with near-zero AOU, which was recently in contact with the atmosphere.

Given the small domain of calculation and the possible effects of the boundary conditions, these results must be interpreted with caution. Nevertheless, the kinematic deformation of the front and the induced vertical circulation appear to be an important process in setting the biogeochemical and hydrographic distribution at the front.

### 7.2. Generalization

This study was performed close to the sea ice edge, but in open waters where wind can directly inject momentum to the ocean. The frontal dynamics in the marginal ice zone or in the pack ice probably differs from that described here. However, our observations of turbulence production at a front close to the marginal ice zone can be a common occurrence in the Atlantic sector of the Arctic. Another surface temperature front was crossed by a Seaglider that was deployed during the cruise (Figure 11a, black trajectory), and its location is in good agreement with the sea surface temperature (SST) maps from satellite observations (Figure 11). The front was located around 81.5°N, 19.5°E and was sampled on 27 September 2018 (cf. Figure 11a). Temperature and salinity profiles (Figures 11b and 11c) collected by the glider show very similar structures to the profiles from the front study: a warm layer at around 25 m depth and a cold layer at about 50 m depth (Figures 6 and 11). Also, a week before the glider crossed the front, the wind blew steadily for 3–4 days from the northeast (not shown), in approximately down-front direction, resulting in similar atmospheric conditions as encountered during our study. $q_g$ calculated from the glider data is negative (not shown); hence, we can speculate that the front crossed by the glider shows similar dynamics (convection due to heat loss to the atmosphere, mechanical forcing by moderate wind, substantial EBF, and FSI). As the front is visible in the SST map in a broad region north of Svalbard, one can suggest that the frontal structure is likely active all along the front north of Svalbard.

### 7.3. Comparison with Other Fronts

Frontal processes are not well documented in the Arctic, but the existing studies suggest energetic turbulence and mixing at frontal systems. Von Appen et al. (2018) observed a submesoscale filament in the marginal ice zone in Fram Strait. This filament was characterized by a strong ageostrophic circulation that

accumulated sea ice and had local subduction of more than 50 m day$^{-1}$, much larger than what is observed at our front (around 5 m day$^{-1}$), impacting mixing, sea ice, and biological productivity.

Compared to the Gulf Stream where FSI is one of the main sources for turbulent kinetic energy production and dissipation, in this study the FSI is a possible source of turbulence complementary to convection. Dissipation is increased at the front as suggested in Johnston et al. (2011), who studied a coastal upwelling front in the California Current, where the ageostrophic vertical velocity was on the order of 2 m day$^{-1}$. In the Arctic front, the increase in dissipation rate is not only located at the front but also in its vicinity because of convection. Johnston et al. (2011) showed that the thermal eddy diffusivity increases from the anticyclonic to the cyclonic side of the front. In our observations, the anticyclonic side is the cold side ($R_0 = -0.8 < 0$), and the increase in dissipation rate and in heat fluxes on the warm side close to the front is consistent with Johnston et al. (2011). Similar to Johnston et al. (2011), the eddy diffusivity in our observations increases from the anticyclonic to the cyclonic side (from $10^{-5}$ m$^2$ s$^{-1}$ to $10^{-3}$ m$^2$ s$^{-1}$ on the cold and warm side, respectively). Relatively large diffusivity is consistent with a deeper reaching mixing on the warm side. Cross-front variability of diffusivity and of the associated heat fluxes could lead to lateral divergence of the vertical heat flux, which could affect the temperature distribution across the front.

In our data set, conditions were favorable for forced symmetric instability during fairly steady, moderate down-front winds. Thomas et al. (2016) investigated how the interaction of inertial oscillations and FSI at a front shapes the stratification, shear, and turbulence in the upper ocean under unsteady forcing during a storm in the Gulf Stream. They showed that FSI more efficiently extracts energy from a front via shear production during periods when inertial motions reduce stratification. During our survey, the wind variability was weak and no evidence of inertial motions were seen. However, storms are strong and frequent in the Arctic and are observed to lead to energetic turbulence and increased heat fluxes (Graham et al., 2019; Meyer, Fer, et al., 2017). The possible contribution of FSI was not addressed in these studies, or in the Arctic fronts in general. FSI is a process that can increase turbulence at the fronts, particularly during storms, and the role of unsteady forcing and inertial motions in Arctic fronts merits further studies.

### 7.4. Impact on Biology

Several studies have suggested the importance of turbulence and mixing on phytoplankton blooms and nutrient fluxes. Blooms are triggered by increased light exposure of the phytoplankton and the development of near-surface stratification that inhibits vertical mixing of the phytoplankton. Mahadevan et al. (2012) showed that the springtime phytoplankton blooms in the subpolar North Atlantic can be initiated by eddy-driven slumping of the basin-scale north-south density gradient. At a front, mixing is inhibited by frontal restratification, and a critical turbulence level is reached that can trigger a phytoplankton bloom (Taylor & Ferrari, 2011). Johnston et al. (2011) showed that at a front in the Californian Current, time scales for mixing and nutrient fluxes were less than 1 day, similar to phytoplankton growth rates. In our study, a subsurface chlorophyll $a$ fluorescence maximum was observed on the cold side of the front, beneath the cold and fresh surface mixed layer. The subduction pattern of this layer was consistent with the downwelling inferred from the cross-front secondary circulation. The AOU below this layer on the cold side reached zero, suggesting a water patch, which was recently in contact with the surface. Measurements of the vertical extent of the euphotic layer and nutrients are needed to firmly establish the impact on biology during our observations. However, our measurements suggest that increased mixing induced by the FSI and convection could enhance nutrient fluxes toward the surface and maintain a phytoplankton bloom above the Atlantic origin water close to the sea ice edge.

## 8. Summary

We investigated an Arctic surface temperature and salinity front using observations in the upper 100 m. The front was extensively sampled on 18 September 2018 near the sea ice edge in the Nansen Basin during fairly steady conditions, with moderate down-front wind. The sampled area was relatively small ($\sim 5 \times 5$ km) due to operational constraints of the AUV. The survey area is comparable to the Rossby radius of deformation (3–10 km), and addresses the submesoscale to turbulent scales.

The surface front was caused by sea ice melt while a deeper front separated Atlantic Water originating from Fram Strait from warm waters that have already recirculated in the Arctic. Intrusive layers were observed at ~35 m (a warm intrusion) and at ~55 m (a cold layer). In the mixed layer, chlorophyll $a$ fluorescence

was larger on the warm side than on the cold side. On the cold side, the local maximum of chlorophyll *a* fluorescence was located below the cold mixed layer, colocated with a deepening of the isopycnals. Vertical velocities calculated using the quasi-geostrophic $\omega$ equation showed a downwelling on the warm side of about 8 m day$^{-1}$ and an upwelling on the cold side of about 4 m day$^{-1}$.

Dissipation rates reached $5 \times 10^{-8}$ W kg$^{-1}$ in the upper 40 m. The main source of turbulence in the front system was the atmospheric forcing by convection and wind stress. At the front, the conditions were favorable for FSI, which could account for the observed increased dissipation rates below the mixed layer depth that could not be explained by the surface buoyancy forcing. Vertical heat fluxes were variable across the front and reached 10 W m$^{-2}$ on the warm side.

Although the dynamics of fronts are well understood in the midlatitude open ocean, our limited data set is the first description of such a system in the Arctic Ocean, covering from submesoscale to turbulent scales. The temperature front was seen in satellite images along the continental slope at the interface between the warm Atlantic Water and the colder waters from the interior of the basin. The frontal processes resolved in our study may be representative of the surface freshwater front north of Svalbard. The front is associated with increased turbulence and vertical heat fluxes and can be important for exchanges of heat between the continental slope and the interior of the basin. Further investigation is needed to quantify the importance of frontal processes and submesoscale-to-turbulence transitions for the heat exchange processes in the deep Arctic Basin.

**Acknowledgments**
This work was supported by the Nansen Legacy Project, Project 276730. We thank the officers, crew, and the other members of the physical oceanography team A. Bosse, E. Falck, B. Lincoln, M. Marnela, F. Nilsen and R. Skogseth, of the *R/V Kronprins Haakon* cruise in September 2018. We thank A. Pietri for providing us with a solver for the $\omega$-equation and M. Müller for the net radiation measurements during the cruise. Insightful and constructive comments from two reviewers helped improve a previous version of this manuscript. The data are available from the Norwegian Marine Data Centre (https://doi.org/10.21335/NMDC-2039932526).

## References

Aagaard, K. (1989). A synthesis of the Arctic Ocean circulation. *Rapp. P.-V. Reun.- Cons. Int. Explor. Mer*, *188*, 11–22.

Athanase, M., Sennéchael, N., Garric, G., Koenig, Z., Boles, E., & Provost, C. (2019). New hydrographic measurements of the upper Arctic western Eurasian basin in 2017 reveal fresher mixed layer and shallower warm layer Than 2005–2012 climatology. *Journal of Geophysical Research: Oceans*, *124*, 1091–1114. https://doi.org/10.1029/2018JC014701

Carmack, E., Polyakov, I., Padman, L., Fer, I., Hunke, E., Hutchings, J., et al. (2015). Toward quantifying the increasing role of oceanic heat in sea ice loss in the new Arctic. *Bulletin of the American Meteorological Society*, *96*(12), 2079–2105. https://doi.org/10.1175/BAMS-D-13-00177.1

Crews, L., Sundfjord, A., Albretsen, J., & Hattermann, T. (2018). Mesoscale eddy activity and transport in the Atlantic water inflow region north of Svalbard. *Journal of Geophysical Research: Oceans*, *123*, 201–215. https://doi.org/10.1002/2017JC013198

D'Asaro, E. A. (1988). Observations of small eddies in the Beaufort Sea. *Journal of Geophysical Research*, *93*(C6), 6669–6684. https://doi.org/10.1029/JC093iC06p06669

D'Asaro, E., Lee, C., Rainville, L., Harcourt, R., & Thomas, L. (2011). Enhanced turbulence and energy dissipation at ocean fronts. *Science*, *332*(6027), 318–322. https://doi.org/10.1126/science.1201515

Dosser, H. V., & Timmermans, M. L. (2018). Inferring circulation and lateral eddy fluxes in the Arctic Ocean's deep Canada Basin using an inverse method. *Journal of Physical Oceanography*, *48*(2), 245–260. https://doi.org/10.1175/JPO-D-17-0190.1

Fer, I. (2009). Weak vertical diffusion allows maintenance of cold halocline in the central Arctic. *Atmospheric and Oceanic Science Letters*, *2*(3), 148–152. https://doi.org/10.1080/16742834.2009.11446789

Fer, I. (2014). Near-inertial mixing in the central Arctic Ocean. *Journal of Physical Oceanography*, *44*(8), 2031–2049. https://doi.org/10.1175/JPO-D-13-0133.1

Fer, I., & Drinkwater, K. (2014). Mixing in the Barents Sea Polar Front near Hopen in spring. *Journal of Marine Systems*, *130*, 206–218. https://doi.org/10.1016/j.jmarsys.2012.01.005

Fer, I., Koenig, Z., Kolås, E., Falck, E., Fossum, T., Ludvigsen, M., Marnela, M.Nilsen, F.Norgren, P. & Skogseth, R. (2019). Physical oceanography data from the cruise KH 2018709 with R.V. Kronprins Haakon, 12-24 September 2018. *Data Set*. https://doi.org/10.21335/NMDC-2039932526

Fer, I., Müller, M., & Peterson, A. K. (2015). Tidal forcing, energetics, and mixing near the Yermak Plateau. *Ocean Science*, *11*, 287–304. https://doi.org/10.5194/os-11-287-2015

Fine, E. C., MacKinnon, J. A., Alford, M. H., & Mickett, J. B. (2018). Microstructure observations of turbulent heat fluxes in a warm-core Canada basin eddy. *Journal of Physical Oceanography*, *48*(10), 2397–2418. https://doi.org/10.1175/JPO-D-18-0028.1

Fossum, T. O., Eidsvik, J., Ellingsen, I., Alver, M. O., Fragoso, G. M., Johnsen, G., & Rajan, K. (2018). Information-driven robotic sampling in the coastal ocean. *Journal of Field Robotics*, *35*(7), 1101–1121. https://doi.org/10.1002/rob.21805

Frajka-Williams, E., Eriksen, C. C., Rhines, P. B., & Harcourt, R. R. (2011). Determining vertical water velocities from Seaglider. *Journal of Atmospheric and Oceanic Technology*, *28*(12), 1641–1656. https://doi.org/10.1175/2011jtecho830.1

Garau, B., Ruiz, S., Zhang, W. G., Pascual, A., Heslop, E., Kerfoot, J., & Tintoré, J. (2011). Thermal lag correction on Slocum CTD glider data. *Journal of Atmospheric and Oceanic Technology*, *28*(9), 1065–1071. https://doi.org/10.1175/jtech-d-10-05030.1

Graham, M., Itkin, P., Meyer, A., Sundfjord, A., Spreen, G., Smedsrud, L., & Granskog, M. (2019). Winter storms accelerate the demise of sea ice in the Atlantic Sector of the Arctic Ocean. *Scientific Reports*, *9*, 9222. https://doi.org/10.1038/s41598-019-45574-5

Gregg, M., D'Asaro, E., Riley, J., & Kunze, E. (2018). Mixing efficiency in the ocean. *Annual Review of Marine Science*, *10*, 443–473. https://doi.org/10.1146/annurev-marine-121916-063643

Guthrie, J., Morison, J. H., & Fer, I. (2013). Revisiting internal waves and mixing in the Arctic Ocean. *Journal of Geophysical Research: Oceans*, *118*, 3966–3977. https://doi.org/10.1002/jgrc.20294

Hoskins, B., Draghici, I., & Davies, H. (1978). A new look at the $\omega$-equation. *Quarterly Journal of the Royal Meteorological Society*, *104*(439), 31–38. https://doi.org/10.1002/qj.49710443903

Jakobsson, M., Mayer, L., Coakley, B., Dowdeswell, J. A., Forbes, S., Fridman, B., & Weatherall, P. (2012). The International Bathymetric Chart of the Arctic Ocean (IBCAO) Version 3.0. *Geophysical Research Letters*, *39*, L12609. https://doi.org/10.1029/2012gl052219

Johnston, T., Rudnick, D., & Pallás-Sanz, E. (2011). Elevated mixing at a front. *Journal of Geophysical Research*, *116*, C11033. https://doi.org/10.1029/2011jc007192

Kumar, B. P., Cronin, M. F., Joseph, S., Ravichandran, M., & Sureshkumar, N. (2017). Latent heat flux sensitivity to sea surface temperature: Regional perspectives. *Journal of Climate*, *30*(1), 129–143. https://doi.org/10.1175/JCLI-D-16-0285.1

Lee, D. K., Niiler, P., Warn-Varnas, A., & Piacsek, S. (1994). Wind-driven secondary circulation in ocean mesoscale. *Journal of Marine Research*, *52*(3), 371–396. https://doi.org/10.1357/0022240943077037

Lenn, Y. D., Rippeth, T. P., Old, C. P., Bacon, S., Polyakov, I., Ivanov, V., & Hölemann, J. (2011). Intermittent intense turbulent mixing under ice in the Laptev Sea continental shelf. *Journal of Physical Oceanography*, *41*(3), 531–547. https://doi.org/10.1175/2010JPO4425.1

Lombardo, C. P., & Gregg, M. C. (1989). Similarity scaling of viscous and thermal dissipation in a convecting boundary layer. *Journal of Geophysical Research*, *94*, 6273–6284.

Mahadevan, A., D'Asaro, E., Lee, C., & Perry, M. J. (2012). Eddy-driven stratification initiates North Atlantic spring phytoplankton blooms. *Science*, *337*(6090), 54–58. https://doi.org/10.1126/science.1218740

Manley, T., & Hunkins, K. (1985). Mesoscale eddies of the Arctic Ocean. *Journal of Geophysical Research*, *90*(C3), 4911–4930. https://doi.org/10.1029/JC090iC03p04911

May, B. D., & Kelley, D. E. (2001). Growth and steady state stages of thermohaline intrusions in the Arctic Ocean. *Journal of Geophysical Research*, *106*(C8), 16,783–16,794. https://doi.org/10.1029/2000JC000605

McDougall, J., & Barker, P. (2011). Getting started with TEOS-10 and the Gibbs Seawater (GSW) Oceanographic Toolbox, 28pp., SCOR/IAPSO WG127, ISBN 978-0-646-55621-5. (Tech. Rep.)

McPhee, M. G. (1992). Turbulent heat flux in the upper ocean under sea ice. *Journal of Geophysical Research*, *97*, 5365–5379.

Meyer, A., Fer, I., Sundfjord, A., & Peterson, A. K. (2017). Mixing rates and vertical heat fluxes north of Svalbard from Arctic winter to spring. *Journal of Geophysical Research: Oceans*, *122*, 4569–4586. https://doi.org/10.1002/2016JC012441

Meyer, A., Sundfjord, A., Fer, I., Provost, C., Villacieros Robineau, N., Koenig, Z., et al. (2017). Winter to summer oceanographic observations in the Arctic Ocean north of Svalbard. *Journal of Geophysical Research: Oceans*, *122*, 6218–6237. https://doi.org/10.1002/2016JC012391

Müller, M., Batrak, Y., Kristiansen, J., Kø, M. A. O., Noer, G., & Korosov, A. (2017). Characteristics of a convective-scale weather forecasting system for the European Arctic. *Monthly Weather Review*, *145*(12), 4771–4787. https://doi.org/10.1175/mwr-d-17-0194.1

Nasmyth, P. W. (1970). *Ocean turbulence*. Diss. University of British Columbia.

Osborn, T. R. (1980). Estimates of the local rate of vertical diffusion from dissipation measurements. *Journal of Physical Oceanography*, *10*(1), 83–89.

Padman, L., & Dillon, T. M. (1987). Vertical heat fluxes through the Beaufort Sea thermohaline staircase. *Journal of Geophysical Research*, *92*(C10), 10,799–10,806. https://doi.org/10.1029/JC092iC10p10799

Padman, L., & Dillon, T. M. (1991). Turbulent mixing near the Yermak Plateau during the coordinated Eastern Arctic Experiment. *Journal of Geophysical Research*, *96*(C3), 4769–4782. https://doi.org/10.1029/90JC02260

Padman, L., & Erofeeva, S. (2004). A barotropic inverse tidal model for the Arctic Ocean. *Geophysical Research Letters*, *31*, L02303. https://doi.org/10.1029/2003GL019003

Padman, L., Levine, M., Dillon, T., Morison, J., & Pinkel, R. (1990). Hydrography and microstructure of an Arctic cyclonic eddy. *Journal of Geophysical Research*, *95*(C6), 9411–9420. https://doi.org/10.1029/JC095iC06p09411

Pollard, R. T., & Regier, L. A. (1992). Vorticity and vertical circulation at an ocean front. *Journal of Physical Oceanography*, *22*(6), 609–625. https://doi.org/10.1175/1520-0485(1992)022<0609:VAVCAA>2.0.CO;2

Polyakov, I. V., Padman, L., Lenn, Y. D., Pnyushkov, A., Rember, R., & Ivanov, V. V. (2019). Eastern Arctic Ocean diapycnal heat fluxes through large double-diffusive steps. *Journal of Physical Oceanography*, *49*(1), 227–246. https://doi.org/10.1175/Jpo-D-18-0080.1

Rainville, L., & Winsor, P. (2008). Mixing across the Arctic Ocean: Microstructure observations during the Beringia 2005 expedition. *Geophysical Research Letters*, *35*, L08606. https://doi.org/10.1029/2008GL033532

Rippeth, T. P., Lincoln, B. J., Lenn, Y. D., Green, J. A. M., Sundfjord, A., & Bacon, S. (2015). Tide-mediated warming of Arctic halocline by Atlantic heat fluxes over rough topography. *Nature Geosci*, *8*(3), 191–194. https://doi.org/10.1038/ngeo2350

Rudels, B., Korhonen, M., Schauer, U., Pisarev, S., Rabe, B., & Wisotzki, A. (2015). Circulation and transformation of Atlantic water in the Eurasian Basin and the contribution of the Fram Strait inflow branch to the Arctic Ocean heat budget. *Progress in Oceanography*, *132*, 128–152. https://doi.org/10.1016/j.pocean.2014.04.003

Rudels, B., Meyer, R., Fahrbach, E., Ivanov, V., Østerhus, S., Quadfasel, D., & Woodgate, R. (2000). Water mass distribution in Fram Strait and over the Yermak Plateau in summer 1997. *Annales Geophysicae*, *18*(6), 687–705.

Shibley, N. C., Timmermans, M. L., Carpenter, J. R., & Toole, J. M. (2017). Spatial variability of the Arctic Ocean's double-diffusive staircase. *Journal of Geophysical Research: Oceans*, *122*, 980–994. https://doi.org/10.1002/2016JC012419

Sirevaag, A., & Fer, I. (2012). Vertical heat transfer in the Arctic Ocean: The role of double-diffusive mixing. *Journal of Geophysical Research*, *117*, C07010. https://doi.org/10.1029/2012jc007910

Sousa, A., Madureira, L., Coelho, J., Pinto, J., Pereira, J., Sousa, J. B., & Dias, P. (2012). LAUV: The man-portable autonomous underwater vehicle. *IFAC Proceedings Volumes*, *45*(5), 268–274. https://doi.org/10.3182/20120410-3-PT-4028.00045

Taylor, J. R., & Ferrari, R. (2009). On the equilibration of a symmetrically unstable front via a secondary shear instability. *Journal of Fluid Mechanics*, *622*, 103–113. https://doi.org/10.1017/S0022112008005272

Taylor, J. R., & Ferrari, R. (2010). Buoyancy and wind-driven convection at mixed layer density fronts. *Journal of Physical Oceanography*, *40*(6), 1222–1242.

Taylor, J. R., & Ferrari, R. (2011). Ocean fronts trigger high latitude phytoplankton blooms. *Geophysical Research Letters*, *38*, L23601. https://doi.org/10.1029/2011GL049312

Thomas, L. N., & Joyce, T. (2010). Subduction on the northern and southern flanks of the Gulf Stream. *Journal of Physical Oceanography*, *40*, 2. https://doi.org/10.1175/2009JPO4187.1

Thomas, L. N., & Taylor, J. (2010). Reduction of the usable wind-work on the general circulation by forced symmetric instability. *Geophysical Research Letters*, *37*, L18606. https://doi.org/10.1029/2010GL044680

Thomas, L. N., Taylor, J. R., D'Asaro, E. A., Lee, C. M., Klymak, J. M., & Shcherbina, A. (2016). Symmetric instability, inertial oscillations, and turbulence at the Gulf Stream front. *Journal of Physical Oceanography*, *46*(1), 197–217. https://doi.org/10.1175/JPO-D-15-0008.1

Thomas, L. N., Taylor, J. R., Ferrari, R., & Joyce, T. M. (2013). Symmetric instability in the Gulf Stream. *Deep Sea Research Part II: Topical Studies in Oceanography*, *91*, 96–110. https://doi.org/10.1016/j.dsr2.2013.02.025

von Appen, W. J, Wekerle, C., Schourup-Kristensen, V., Konrad, C., & Iversen, M. H. (2018). Observations of a submesoscale cyclonic filament in the marginal ice zone. *Geophysical Research Letters*, *45*, 6141–6149. https://doi.org/10.1029/2018GL077897

Zhao, M., Timmermans, M. L., Cole, S., Krishfield, R., Proshutinsky, A., & Toole, J. (2014). Characterizing the eddy field in the Arctic Ocean halocline. *Journal of Geophysical Research*, *119*, 8800–8817. https://doi.org/10.1002/2014jc010488